Chapter 19
Metal Nanocatalysts

Yuanyuan Li and Anatoly I. Frenkel

19.1 Introduction

Metal nanoparticles (NPs) under several tens of nanometers in size have unique mechanical, optical, electronic, and catalytic properties that are different from their bulk counterparts [1–5]. Structural characterization of NPs is a key to answering many questions related to their catalytic properties, for example, what is the nature of catalytically active sites, or what are the reasons for their catalytic activity, selectivity, and stability. Various structural, geometric, and electronic characteristics were named "descriptors" of catalytic properties in transition metal catalysts, such as the number of under-coordinated sites [6, 7], or perimeter sites [7, 8], or number of (111) crystalline facets [9], or surface strain [10], or the position of the D-states relative to the Fermi level (a "D-band center" model) [11–15]. The main challenge preventing direct measurements of those characteristics is the small size of nanoparticles. Indeed, in size range of several nanometers, there are very few techniques capable of characterizing structure and electronic properties with sufficient spatial and energy resolutions. A challenge specific to catalysts is the need to monitor their structure and electronic properties in situ, during their work, also known as "in *operando* conditions." That latter requirement is particularly challenging to electron microscopy and other imaging techniques that are severely limited in use by requirements of high pressure and temperature, typical for many catalytic reactions. Other structural characterization techniques such as X-ray diffraction are limited by the small size of the nanoparticles that is responsible for broadening Bragg peaks used for structural refinement. XAFS analysis methods are excellent alternatives to imaging and scattering methods due to the excellent spatial, temporal, and energy resolutions of XAFS, and due to the relative ease of its

Y. Li • A.I. Frenkel (✉)
Department of Physics, Yeshiva University, New York, NY 10016, USA
e-mail: anatoly.frenkel@yu.edu

Y. Iwasawa et al. (eds.), *XAFS Techniques for Catalysts, Nanomaterials, and Surfaces*, DOI 10.1007/978-3-319-43866-5_19

application to real-time processes in *operando* conditions. In recent years, it became progressively more appreciated that supported NPs are complex systems whose catalytic properties are influenced not only by the structure of the particle but also in not a small degree by its interaction with support and adsorbates. In this chapter, we review the main attributes of supported NPs that affect their catalytic activities, recent solutions to the structural characterization of NPs and describe recent advances in solving three-dimensional structure, degree of alloying, and their changes under conditions of model and real catalytic reactions.

19.2 Size, Shape, Strain, Support, and Composition Effects on Catalytic Properties

With the decrease of particle size, the surface to volume ratio increases, shifting the balance between the surface and the bulk energies in favor of the former. Enhanced surface energy is responsible for generating substantial surface strain [16, 17], that can be relieved by some adsorbates, e.g., hydrogen [5, 18, 19]. The enhanced surface stress causes contraction of surface metal–metal bond length [16, 20, 21]. The surface energy and surface stress thus have important influence on the elastic properties of NPs.

In nanocatalysts strain is a ubiquitous attribute of their structure. It dominates the surface and support interface regions, and, in the case of bimetallics, is also present throughout the bulk, due to the size mismatch of two types of metals [10, 16, 22–25]. The increased surface strain results in the shift of D-band center [10, 26–28] which tunes the binding energy between surface atoms and adsorbed molecules [10–12], and changes cohesive energy of surface atoms which alters the thermodynamic properties and stiffness of NPs [17, 29].

Electronic structure of NPs could also be modified through the change of particle size. Lowering the coordination number of NPs causes the tendency towards localization of the valence electrons and gap formation, hence, the transition from metallic (at large sizes) to nonmetallic (in small sizes) properties. Another consequence of decreasing particle size is thus the reduction of the width of valence band and the shift of its center of gravity towards Fermi level which leads to an increase of the adsorption energy of adsorbate and a decrease of the dissociation barriers of adsorbed molecules [13, 14, 30]. For transition metals catalysts, their properties could thus be tailored through the D-band center position relative to the Fermi energy by changing the composition (adding different metal atoms) [13, 15, 31], surface strain, support material [32–35], or adsorbate coverage [12].

NPs with various shapes expose different facets, which may have different properties with respect to catalysis in the course of the same reaction [36, 37]. In addition, different surface types contain different fractions of under-coordinated atoms (on edge and vertex), which are considered to be the active sites in many reactions [6–9]. Shapes of NPs are shown to change with size [38], however, when

particles are extremely small, and they could adopt various geometries with comparable energies. The fluctuation of geometries and structures could lower the reaction barrier [39, 40]. Finally, the nanoparticles can coexist in the ordered and disordered states in the same size range, and their fractions can change in reaction condition, further hampering efforts in their characterization and thus understanding catalytic mechanisms [18].

Most heterogeneous nanocatalysts are deposited on supports, which distort the atomic structure of the interfacial layer in contact with the substrate, creating defects, strain at interface and may even change the shape of NPs [22, 32, 33]. On the other side, supports with different reducibility have different influences on the electronic structure of NPs. These structural and electronic factors control the metal/support adhesion energy, which affects chemical potentials of surface atoms and their binding ability to small adsorbates [35].

The addition of the second metal to monometallic systems was found to be an effective way to tune the properties and structures of nanocatalysts. The possible mixing patterns of bimetallic systems reported in literature vary from random alloys, core–shell, cluster-by-cluster, and other architectures, depending on the elements, their compositions and synthesis conditions [41, 42]. The introduction of the second metal could introduce strain, alter the electronic structure and, hence, the d-band center position, which greatly affects the interaction between the surface atoms and adsorbates. Many bimetallic systems were reported to change their structure and/or compositional motifs in response to the changes in the environmental conditions or in the process of catalytic reactions [43–45]. Tracking the structural changes of bimetallic systems *in operando* mode, that is, during real reaction conditions, while monitoring the reaction in real time, is thus quite important for revealing their working mechanisms.

19.3 Experimental Characterization of Nanoparticle Structure and Electronic Properties: The Uniqueness of XANES and EXAFS

X-ray diffraction (XRD), X-ray photoelectron spectroscopy (XPS), and electron microscopy are commonly used techniques for bulk or surface structure characterization. When particle size is in nanometer range, XRD is not very helpful due to the Bragg peak broadening. Electron microscopy, on the other hand, has very high resolving power, which helps reveal the atomic and surface structure of NPs [46]. However, if used in situ, only part of the ensemble of catalytic species can be reliably detected (above the resolution limit) and reports of applications of TEM to *operando* studies are still scarce. X-ray absorption spectroscopy (XAS), on the other hand, can be done in a number of sample conditions (liquid or gas, low or high temperatures and pressures) [47–52], and a number of reactor cells are available to date [53–57]. Its sensitivity to local structure and elemental specificity make it

uniquely fitting for studying nanomaterials. With the development of the analytical methods for XANES and EXAFS interpretation, a lot of information related to the physical properties of nanomaterials, such as stress-induced bond length change and disorder [19, 22, 58], three-dimensional geometry of small clusters [59, 60], electronic structure modification driven by support/environment [61], and mixing pattern of bimetallic systems [45, 62, 63], could be obtained. In recent years, with the proliferation of in situ and *operando* methods of catalyst characterization, combination of XAFS with other techniques (IR, Raman, XRD, NMR, UV–Vis, etc.) helped illuminate cooperative phenomena at the interfaces between nanoparticle, surface species, and support under realistic working conditions [43, 50, 56, 74–88].

In the following sections, we review recent progress in structural characterization of nanocatalysts by EXAFS methods.

19.4 Size and Geometry of Nanocatalysts by Coordination Number Analysis

Historically, the importance of EXAFS for catalysis studies [89] was realized almost immediately after XAFS was recognized as a new method of studying local structure in 1970s [90–94]. First works used it for measuring coordination numbers of supported monometallic and heterometallic NPs to obtain their average size (only first shell/single scattering analysis was possible) [95–98]. Then, with the development of multiple scattering (in the 1990s) [99] more advanced analysis methods were developed for determination of cluster size, shape, morphology, and mixing pattern in bimetallic systems. Information about the atomic architecture (three-dimensional packing of atoms) in a representative NP can be most directly gleaned from the coordination number of first nearest neighboring metal–metal bonds. The coordination number ($n_{AA(i)}$) of the ith shell with the radius R_i around the absorbing atom in a monometallic cluster is defined as the average number, per absorber, of nearest neighbors within a given shell:

$$n_{AA(i)} = \frac{2N_{\mathrm{AA(i)}}}{N_A}. \tag{19.1}$$

Here $N_{AA(i)}$ is the total number of the A–A nearest neighbors within the same coordination shell, and N_A is the total number of A-type atoms in the cluster. The factor of two in Eq. (19.1) is due to the fact that each atom of the A–A pair is an absorber and thus the number of these pairs should be doubled in calculating the A–A coordination numbers. Coordination numbers are obtained model-independently from data analysis of experimental EXAFS spectra. The most important information that is available via the coordination number analysis is the average particle

size, and several methods are available for its determination from the EXAFS coordination numbers [100].

One such method, developed by Calvin et al. [101], assumes homogeneous spherical shape of clusters with the radius R. For atoms in the *i*th shell around the absorbing atom, the coordination number of the *i*th shell ($N_{nano(i)}$) can be expressed as follows:

$$N_{nano(i)} = \left[1 - \frac{3}{4}\left(\frac{r_i}{R}\right) + \frac{1}{16}\left(\frac{r_i}{R}\right)^3\right] N_{bulk(i)}. \tag{19.2}$$

In Eq. (19.2), r_i is the distance between the absorbing atom and neighboring atoms in the *i*th shell, and $N_{bulk(i)}$ is the *i*th shell coordination number of bulk structure. This method allows the calculation of coordination number of an arbitrary coordination shell as a function of the cluster size, which in principle, can be used to discriminate between symmetric (quasi-spherical) and asymmetric clusters if the coordination numbers of the higher-order shells are measured by EXAFS. One disadvantage of this method is that it is limited to sufficiently large clusters (with number of atoms much larger than 100) [60].

Another useful method for estimating cluster size is comparing the first nearest coordination number (N_1) obtained from EXAFS analysis against model structures with known geometrical characteristics. For regular polyhedra (e.g., a cuboctahedron or an icosahedron), N_1 is a function of cluster order L, which is defined as the number of spacing between adjacent atoms along the edge (see example of $L = 2$ in Fig. 19.1) [102]. This method developed by Montejano-Carrizales et al. [102, 103], is easy to expand to other morphologies and cluster families [59]. For example, the truncated cuboctahedral model with the (111) plane parallel to the support is most close to the morphology found in many supported metal clusters (Fig. 19.1). The relationship between N_1 and L in a truncated cuboctahedron is: [104]

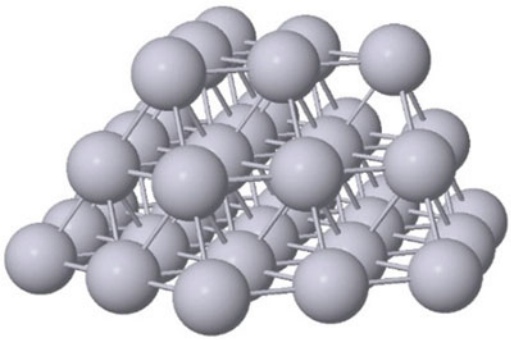

Fig. 19.1 Schematic of a truncated cuboctahedral cluster with 37 atoms ($L = 2$)

$$N_1 = \frac{3\left(20L^3 + 21L^2 + 7L\right)}{5L^3 + 12L^2 + 10L + 3}. \tag{19.3}$$

For truncated cuboctahedron with atom numbers of 10 ($L = 1$), 37 ($L = 2$), 92 ($L = 3$), and 185 ($L = 4$), the first nearest coordination numbers are 4.8, 7.0, 8.2, and 8.9, respectively.

Another method that is useful in the case when there is no particular symmetry known in advance, and/or nearest neighboring shells cannot be easily identified but the coordinates of atoms in the cluster are available from, e.g., first principle simulations, is the radial distribution function (RDF) method [59, 105]. This approach, proposed by Frenkel and Glasner [59], employs computer-generated cluster coordinates. The cluster-average pair radial distribution function $\rho(r)$ is computed for a cluster of N atoms:

$$\rho(r) = \frac{1}{N}\sum_{i=1}^{N}\rho_i(r),\ \rho_i(r) = \frac{dN_i}{dR_i}, \tag{19.4}$$

where $\rho_i(r)$ is the partial RDF for an atom i, and dN_i is the number of its neighbors within the spherical shell of thickness dR_i. The subsequent calculation of coordination numbers for an arbitrary coordination shell (between R_1 and R_2) is achieved by integrating the ρ(r):

$$n_i = \int_{R_1}^{R_2}\rho(r)dr. \tag{19.5}$$

Compared to the two methods described above, the RDF method enables rapid calculation of coordination numbers of clusters with arbitrary sizes and shapes. By combining electron microscopy with multiple-scattering EXAFS analysis and data modeling, several geometries with the same sequence of coordination numbers of the nearest-neighbor shells can be discriminated [106, 107]. The authors can be contacted for sharing their software program that performs RDF calculations for arbitrary cluster geometries.

The methods listed above for size estimation are strongly dependent on the knowledge of the first nearest coordination numbers that are, in turn, obtained reliably by EXAFS analysis if the bond length distribution is relatively symmetric [91, 108]. For supported nanocatalysts under working conditions, the substrate and adsorbates may induce stress, causing the bond length distribution to deviate strongly from the Gaussian shape by for example relaxing the surface atoms stronger compared to the core [16]. The asymmetric disorder in bond lengths results in an artifact of the data analysis where, if ignored, it leads to the underestimate of the coordination numbers [109]. Therefore, anharmonic corrections should be taken into account for systems with large disorders. Several methods have been proposed recently that take into account the asymmetric disorder and use structural analysis of EXAFS data to validate different theoretical models [110–112]. They are described in greater detail below.

Including multiple-scattering effects to EXAFS data analysis is another way to improve the accuracy for size determination and is also crucial for extending structural refinement of nanocatlysts beyond first nearest bond distance. From the geometrical characteristics of regular polyhedral clusters, the sequence of coordination numbers of the 1st, 2nd, 3rd, 4th, etc. nearest neighboring pairs of atoms for different types of polyhedra is unique. That uniqueness is used for comparison with EXAFS results, obtained model-independently, for the same coordination numbers (and for degeneracies of multiple-scattering paths) to determine the size, shape, structure, and, in some cases, surface orientation of NPs [59, 106, 113]. One example of such analysis is the characterization of supported Pt clusters [60, 106, 114, 115], which have been extensively studied by EXAFS to establish the relationship between cluster size, shape, and catalytic properties. The structural characteristics depend strongly on the preparation conditions and on the nature of support [6, 22, 107, 116, 117]. The demonstrations of the sensitivity of the cluster shape to the support and treatment conditions are shown in the following examples. The fully reduced γ-Al_2O_3 supported Pt NPs have a spherical structure through a preparative method of deposition precipitation [118] while PVP capped Pt NPs changed from spherical to flat structure after the particles were deposit on SiO_2 support [119]. In another example, the 1 wt% Pt/γ-Al_2O_3 catalyst containing 11 Pt atoms was three-dimensional after low temperature reduction (300 °C) and changed to the raft shape with the structure similar to Pt (100) after high temperature reduction (450 °C) [120]. Interestingly, for Pt/zeolite, the three-dimensional structure was retained after high temperature treatment [121].

As an example of the multiple scattering EXAFS analysis of the cluster shape, we use the structural modeling of carbon supported Pt NPs up to the 4th/5th Pt-Pt shell [106, 114]. Figure 19.2 illustrates such analysis

for size and shape determination and shows that the (111)-truncated hemispherical cuboctahedron provides good approximation for the 10 wt% Pt/C sample, with a particles size of about 1.7 nm [106]. To find connections between particle shape and catalytic properties, γ-Al_2O_3 supported Pt NPs with various shapes but analogous average size (~1 nm) were prepared and characterized by multiple-scattering analysis (up to 4th shell) of EXAFS data in combination with microscopic tools [107]. The shape having higher percentage of undercoordinated atoms (at edge or corner sites) on the surface was found effective for lowering the onset temperature for two-propanol oxidation [6].

A more approximate method that also relies on the coordination numbers of higher shells for determining the size and shape of NPs was proposed by A. Jentys [122]. This method modeled the first five coordination numbers as a function of particle size with a hyperbolic function for particles with shapes of spheres, cubes, and distorted cubes. The coordination number of the first (n_1) or second shell (n_2) was found independent with shape and thus used to estimate the average particle size. The curves of n_1/n_3 versus particle size were found to be different for different shapes. The shape can therefore be determined by comparing the curve of experimentally determined n_1/n_3 ratio with the model n_1/n_3 graph. Such analysis was expanded by Beale and Weckhuysen to larger number of shapes [123].

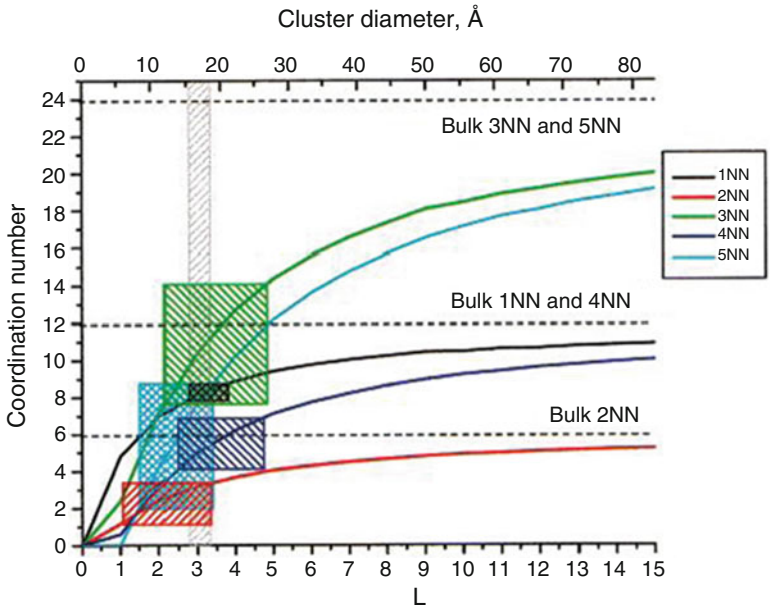

Fig. 19.2 Comparison of the average distances (up to 5NN), together with their error bars (shown as shaded rectangles), measured by EXAFS for the 10 wt% Pt/C sample and the calculated from a truncated (by (111) plane) cuboctahedron for cluster orders L up to 15. Reproduced with permission from ref. [106]. Copyright 2001 American Chemical Society

19.5 Using EXAFS to Characterize Bimetallic Nanocatalysts

Methods of high precision synthesis of bimetallic NPs for catalysis and electrocatalysis are actively sought, due to the increased demand to minimize the use of noble metals and for rational design of catalysts with desired activity and selectivity, and increased stability [42, 124–131]. Analogously to the definition of the coordination number for a homo-metallic pair, for heterometallic bonds, the coordination number is defined as:

$$n_{AB} = \frac{N_{AB}}{N_A}. \tag{19.6}$$

The information on the homo- and hetero-metallic coordination numbers n_{AA}, n_{AB}, n_{BA}, and n_{BB} is available from EXAFS measurements on the absorption edges of both A and B central atoms [25]. The analysis should be done for both edges concurrently, with constraints imposed on the heterometallic bonds during the fits:

$$n_{AB} = \frac{x_B}{x_A} n_{BA},\ R_{AB} = R_{BA},\ \sigma^2_{AB} = \sigma^2_{BA}. \tag{19.7}$$

Just as in the case of monometallic catalysts, multiple-scattering analysis of bimetallic catalysts allows for measurements of coordination numbers within the first few shells [114, 132]. These parameters elucidate the intra-particle composition, such as the extent of segregation or alloying of atoms, e.g., random distribution, as opposed to the positive or negative tendency to clustering [60, 132–140]. Once the above parameters are known, the total coordination number of metal–metal (M-M) neighbors per absorbing atom can be found from: [60]

$$n_{MM} = x_A n_{AM} + x_B n_{BM}. \tag{19.8}$$

The total coordination number can be employed to determine the size and shape using the same methods applied to monometallic particles described above.

For heterogeneouse distributions, the main question in the EXAFS analysis of bimetallic NPs is to detect a certain architectrual motif, e.g., a core–shell or cluster-to-cluster [41, 42, 45]. When atoms of the type A will segregate to the surface of the nanoparticle and B—to the core, then $n_{AM} < n_{BM}$ [60]. For *random* alloys, the average coordination numbers n_{AA} and n_{AB} are in the same proportion as the bulk concentrations of these elements in the sample: [60]

$$\frac{n_{AA}}{n_{AB}} = \frac{x_A}{x_B}. \tag{19.9}$$

For alloys with *positive* tendency to clustering of like atoms, e.g., when either the intraparticle or interparticle segregation is present, the left hand side should be *larger* than the right hand side:

$$\frac{n_{AA}}{n_{AB}} > \frac{x_A}{x_B}. \tag{19.10}$$

For homogeneous alloys (Fig. 19.3, center) in which the atoms A and B occur with equal probability within the particle or on the surface: $n_{AM} = n_{BM}$ [60].

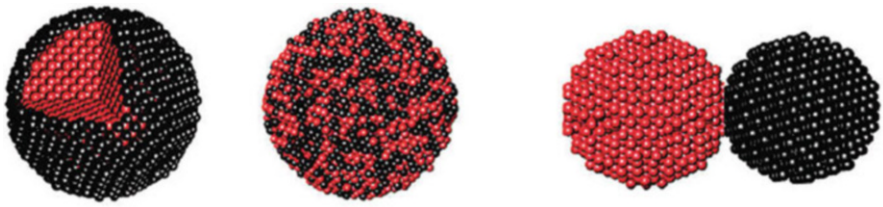

Fig. 19.3 Three main types of bimetallic configuration: left: core–shell; center: alloy; right: segregated monometallic clusters. Reproduced with permission from ref. [45]. Copyright 2009 American Chemical Society

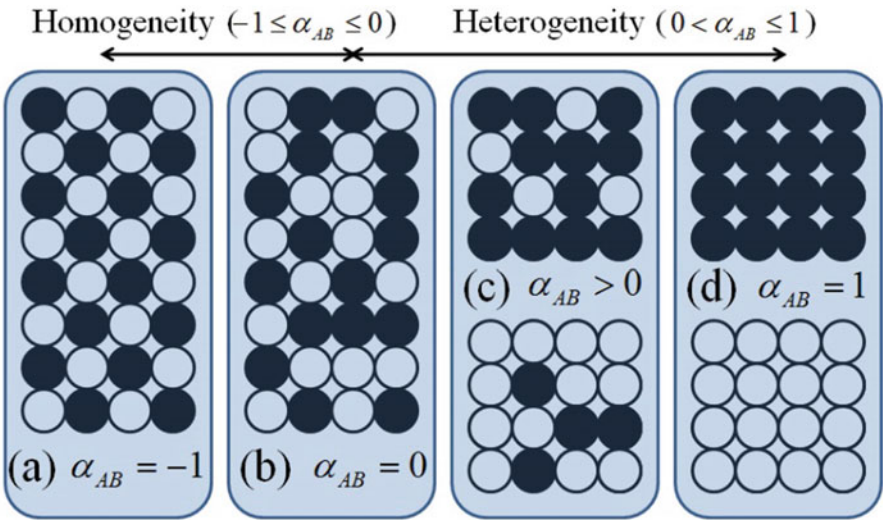

Fig. 19.4 (**a**, **b**) shows homogeneous configurations for the same 50–50 composition, characterized by a unique, non-positive values of the short range order parameter α. Different heterogeneous configurations, characterized by positive values of α, are shown in schemes (**c**, **d**). Reproduced with permission from ref. [62]. Copyright 2013, AIP Publishing LLC

Interpretation of the coordination numbers in heterogeneous systems in terms of a "representative cluster" can be misleading. We will discuss two commonly encountered systems that require particular care. One example is when two different NP systems differ in homogeneity of their atomic distributions, and the other—in the degree of their randomness. First, we consider a homogeneous system where all atoms have similar local environments within each NP. Two cartoons depicting two dimensional "nanoparticles" with this type of structure are shown in the Fig. 19.4a, b. Although the lattices are differently ordered, both types of atoms contain a similar number of neighbors for each element throughout the "cluster." The similarity becomes nearly perfect when the surface to volume ratio becomes negligible, i.e., for particles larger than 4–5 nm in diameter. Such atomic arrangements are homogeneous, as there is an equal probability to find any given atom type (A or B) anywhere within the NP. An example showing the other extreme is presented in the two cartoons in the Fig. 19.4d where the atoms of each type (A or B) are segregated within different part of the NP.

The second case we briefly discuss is when the two NP systems differ in the randomness of their atomic distributions. This characteristic will only apply to the homogeneous systems such as two NPs shown in Fig. 19.4a, b, because the two NPs shown in Fig. 19.4c, d are heterogeneous, i.e., inherently nonrandom. The cluster on the Fig. 19.4a has perfect order: both atomic types have equivalent surroundings. The cluster in Fig. 19.4b is random: for either atom (of type A or B), the probabilities of neighboring atoms being either type A or B are equal. One important consequence apparent from this simple example is the difference between the

short range order and homogeneity. For example, an alloy can be homogeneous but have a "negative tendency to clustering" (i.e., short range order) and is a phenomenon frequently encountered in metallurgy [141, 142].

These two examples illustrate the importance of understanding the short range order and homogeneity of bimetallic NPs when attempting to characterize their structure. It turns out that both of these can be quantitatively expressed using J. Cowley's short range order parameter introduced recently for bimetallic NP analysis by Frenkel, et al.: [143–145]

$$\alpha = 1 - \frac{N_{AB}/N_{AM}}{x_B}, \tag{19.11}$$

where x_B is the molar concentration of B-type atoms in the sample. As we show below, the Cowley parameter (α can vary in the interval between −1 and 1) can be used to investigate the degree of alloying or clustering within bimetallic NPs based on how positive/negative it is. In many cases, it can be used also as a "litmus test" demonstrating that atomic segregation, of either intra-cluster or inter-cluster type, occurred. We note that this equation has been previously employed in EXAFS studies of bulk bimetallic alloys [24] but its potential in NP studies remains unexplored.

For alloys that favor (disfavor) clustering of like atoms, α will be positive (negative). This parameter is therefore essential for studies of alloy—or core–shell, or cluster-on-cluster—NPs that can be characterized by different levels of ordering. Only after the short range order parameter is evaluated, can different models of segregation be compared. In either case, additional experimental information is needed to determine the fine detail of segregation, i.e., whether for example element A is predominantly at the surface or in the core. The analogue of the effect of compositional heterogeneity on the interpretation of the short range order within a "representative" NP is the interpretation of the size of the "representative" NP from EXAFS coordination numbers. In each case, an independent technique is needed, and in the latter case, the average particle size can be measured by electron microscopy.

We emphasize that the role of measuring and evaluating α extends beyond merely determining whether it is positive or negative. Even large negative values of α may signal segregation as there is only a finite range $\alpha_{\min} \le \alpha \le 0$ in which homogeneous systems can exist [143]. For example, $\alpha_{\min} = -1$ for two dimensional AB alloys shown in Fig. 19.4a, for β-brass CuZn of bcc structure [143], but it can also be fractional, e.g., $\alpha_{\min} = -1/3$ for fcc $Cu_{0.75}Au_{0.25}$ alloys [143]. Hence, if the measured value of α falls within either $-1 \le \alpha \le \alpha_{\min}$ or $0 < \alpha \le 1$ interval, the system is heterogeneous and the segregation of atoms is evident. Finally, we note that these conclusions were obtained assuming an idealized case where all particles are equivalent and the segregation may occur only within the NP. If the bimetallic composition varies from one NP to another, even random compositional distribution may generate positive values of α, a point which is discussed in greater detail below.

19.6 Pitfalls and Artifacts of the Analysis

In studies of the structure of NPs, coordination numbers are the most important structural parameters that can be obtained from EXAFS analysis. Coordination numbers of the first nearest neighbors (1NN) of X-ray absorbing atoms are obtained by EXAFS analysis very reliably, and are often employed for characterizing nanoclusters in terms of their structure, size, shape, and morphology [100, 106, 114, 146]. Coordination numbers of atomic pairs in bimetallic NPs are often used to discriminate between different types of short range order in the NPs, and/or ascertain the degree of compositional homogeneity in the sample [60, 100, 147]. In this section we emphasize the pitfalls in such interpretation when nanoparticle ensembles display a broad range of sizes and compositions. We show the implications of these effects on EXAFS results and describe corrective strategies.

The values of partial coordination numbers are important for analyzing composition habits of heterometallic clusters. For example, depending on the relationship between the partial 1NN numbers and the bulk composition of the nanoalloy, the latter is characterized as either homogeneous (when average environment around each atom is approximately the same) or heterogeneous (when different regions within the sample have different compositional trends, e.g., A- rich and B-rich, or when such segregation occurs within each cluster, e.g., A-rich core and B-rich shell) [147]. For homogeneous alloys, relationships (19.9) and (19.10) can be used to describe the short range order [60]. In this section we focus on random nanoalloys (that have zero short range order) and highlight challenges in their detection by EXAFS.

We now introduce the *total* coordination number of metal–metal pair, or n_{MM} which is equal to n_1 for monometallic clusters. For bulk alloys, when atoms of type A and B are distributed *randomly*, their partial coordination numbers are found from the overall compositions:

$$n_{AA} = n_{BA} = x_A n_{MM},\ n_{AB} = n_{BB} = (1 - x_A)\, n_{MM}, \tag{19.12}$$

where the composition is defined as: $x_{\mathrm{A}} = N_{\mathrm{A}}/N$. Note that in random bulk alloys, $n_{\mathrm{AA}} + n_{\mathrm{BB}} = n_{\mathrm{AA}} + n_{\mathrm{AB}} = n_{\mathrm{BB}} + n_{\mathrm{BA}} = n_{\mathrm{MM}}$. In a nanocluster with random compositional distribution, more accurate relationships should be used: [100]

$$\begin{aligned} n_{AA} &= \frac{N_A - 1}{N - 1} n_{MM} = \frac{N x_A - 1}{N - 1} n_{MM},\ n_{AB} = \frac{N - N_A}{N - 1} n_{MM} \\ &= \frac{N}{N - 1}(1 - x_A) n_{MM}, \quad n_{BA} = \frac{N_A}{N - 1} n_{MM} = \frac{N}{N - 1} x_A n_{MM}, \\ n_{BB} &= \frac{N_B - 1}{N - 1} n_{MM} = \left(1 - \frac{N x_A}{N - 1}\right) n_{MM}. \end{aligned} \tag{19.13}$$

We note that in random nanoalloys, same as in the bulk random alloys, $n_{\mathrm{AA}} + n_{\mathrm{AB}} = n_{\mathrm{BB}} + n_{\mathrm{BA}} = n_{\mathrm{MM}}$ but in the nanoalloys the sum of n_{AA} and n_{BB} is smaller than n_{MM}:

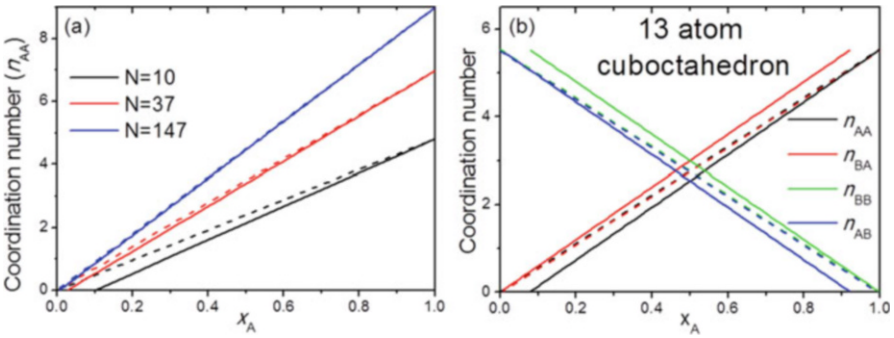

Fig. 19.5 (**a**) Exact (*solid lines*, Eq. 19.13) and approximate (*dashed lines*, Eq. 19.12) behaviors of the coordination numbers of A–A pairs for different cluster sizes. (**b**) Coordination numbers of different atomic pairs in random, 13-atom, cuboctahedral alloys. *Solid lines* correspond to exact calculations using Eq. 19.13 and *dashed lines* correspond to approximate calculations using Eq. 19.12. Reproduced from ref. [149] by permission of The Royal Society of Chemistry

$$n_{AA} + n_{BB} = \frac{N-2}{N-1} n_{MM}. \tag{19.14}$$

Equations (19.13 and 19.14) are exact, and they are equivalent to Eqs. (19.1, 19.6, 19.9, and 19.12) in the limit of large total number of atoms (N) and large concentrations (x_A), as demonstrated in Fig. 19.5a. Furthermore, in the random nanoalloys, the n_{AA} and n_{BB} are different from n_{BA} and n_{AB}, respectively, while in the random bulk alloys they are the same (Eqs. 19.12, 19.13 and Fig. 19.5b).

We have recently shown [100] that alloys with broad compositional distributions are expected to have positive values for the ensemble-average short range order despite having random intra-particle distribution of atoms. Hence, a random nanoalloy may be mistaken as a system with a core–shell motif if the NPs are not all stoichiometrically uniform. This prediction can be illustrated by the following simple example. Assume that the sample consists of two groups of bimetallic NPs. The first group consists of N particles where 30 % of all atoms are A-type and 70 %—B-type in each. The second group consists of N particles of 70 % and 30 % of A and B-type atoms, respectively. The average composition over the entire sample is then 50 % of A and 50 % of B atoms. Assume also that the distribution of atoms in each particle is random, i.e., the value of α calculated over each population is zero. Finally, assume that the geometry of all particles is the same and atoms occupy regular lattice sites. Ensemble-average calculation of the coordination numbers of AB type yields the following result: $N_{AB} = 0.3 \times 0.7 N_{AM} + 0.7 \times 0.3 N_{AM} = 0.42 N_{AM}$. Hence, the ensemble-average value of α measured by EXAFS will be equal to 0.16 (Eq. 19.11), in apparent contradiction to the local randomness ($\alpha = 0$) of each population. What follows is the more general demonstration of this effect [100, 148].

We assume that within each cluster, atoms of type A and B are distributed randomly, but x_A is different for each nanoparticle. For simplicity, we consider a

system that contains particles of the same structure and geometry. Effects of cluster size distribution [100] and asymmetric bond length disorder [109] on the apparent coordination numbers have been described separately. We distinguish between the particle-specific coordination number n_{AA} (calculated with Eq. (19.13)) in the cluster with the concentration x_A of A atoms, and the *apparent* (measured) coordination number $\widetilde{n}_{AA}$, which, in EXAFS measurement, averages the number of A nearest neighbors over all the A-type atoms in all clusters in the sample. We let the interparticle compositional distribution of x_A (denoted below as simply x) be a Gaussian with standard deviation σ_c and mean $\bar{x}$:

$$\rho(x) \propto \exp\left(-\frac{(x-\bar{x})^2}{2\sigma_c^2}\right). \tag{19.15}$$

In EXAFS signal, clusters with a greater number of A atoms are weighted more than the clusters with fewer A atoms. We thus write the apparent partial coordination numbers as:

$$\widetilde{n}_{AA} = \frac{\int_0^1 \rho(x) n_{AA}(x) x dx}{\int_0^1 \rho(x) x dx}. \tag{19.16}$$

Figure 19.6 shows the values of $\widetilde{n}_{AA}$ and $\widetilde{n}_{AA}$ for various values of $\bar{x}$ and σ_c calculated for a cluster containing $N = 100$ atoms. Cluster cartoons are added for clarity. A single cluster (the cuboctahedral shape was chosen for illustration purpose

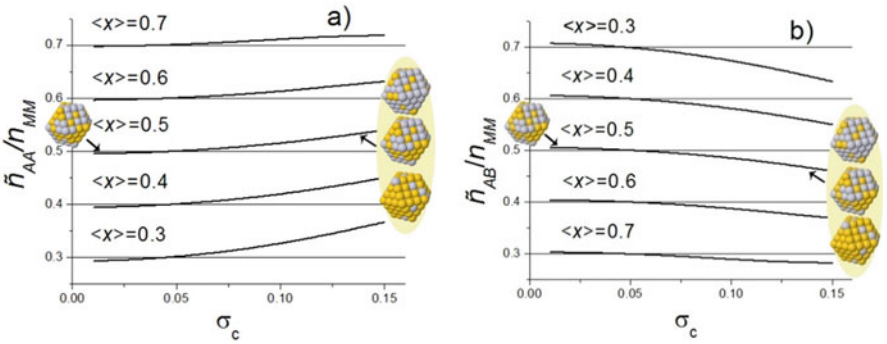

Fig. 19.6 Normalized partial coordination numbers of (**a**) *AA* and (**b**) *AB* pairs as functions of the standard deviation σ_c around the average cluster composition $<x>$ for clusters of $N = 100$ atoms, calculated assuming a Gaussian compositional distribution. In both figures, cartoons next to the $< x >= 0.5$ curve illustrate the difference between the narrow (one cluster on the left) and broad (three different clusters on the right) compositional distributions. Reproduced from ref. [148] by permission of The Royal Society of Chemistry

only) on the left corresponds to narrow inter-cluster compositional distribution (i.e., small σ_c). Three clusters on the right illustrate the change in composition from cluster to cluster (large σ_c). In all cases, the intra-cluster distributions are random.

These results indicate that the ensemble-average coordination numbers $\widetilde{n}_{AA}$ can be smaller for narrow compositional distributions or larger for broad distributions than the coordination numbers predicted by the equation $n_{\mathrm{AA}} = xn_{\mathrm{MM}}$. The reason they are smaller for narrow distributions than the nominal coordination numbers was demonstrated above (Eq. 19.13 and Fig. 19.5b). For broad distributions, the effect is due to the ensemble-averaging that favors A-rich clusters over the B-rich clusters (relative to $\bar{x}_{\mathrm{A}}$). Similar conclusions can be extended to the other partial coordination numbers. The two sets of values, $\widetilde{n}_{AA}$ and n_{AA}, as well as $\widetilde{n}_{AB}$ and n_{AB}, agree for $\sigma_c = \sqrt{x(1-x)/N}$, for which the normal distribution coincides with binomial distribution.

In summary, partial coordination numbers in heterometallic NPs can be employed to accurately quantify the intra-particle homogeneity and short-range order for arbitrary cluster sizes and a wide range of component fractions, provided that all the clusters possess nearly identical compositions. If the intra-cluster distribution is completely random but the elemental composition varies widely from cluster to cluster, the coordination numbers measured by EXAFS will point toward either negative ($\widetilde{n}_{AA} < n_{AA}$) or positive ($\widetilde{n}_{AA} > n_{AA}$) short range order, which, in the latter case, can be mistaken for a core–shell motif, among other segregation scenarios, even though all clusters are completely random. The only exception when the apparent coordination numbers coincide with those in the "mean" cluster is when the compositional distribution is binomial. With the knowledge of actual compositional distribution (e.g., using energy dispersive X-ray analysis done in electron microscopy experiment) it is possible to correct apparent coordination numbers for the compositional distribution effects (Fig. 19.6).

19.7 Overlapping Absorption Edges

Heterometallic systems containing two or more elements with overlapping absorption edges cannot be simply analyzed by EXAFS since the EXAFS at the higher energy edge overlaps with the EXAFS extending from the lower energy edge. This is a particularly significant problem for metals that neighbor each other in the periodic table such as Re, Ir, Pt, and Au, whose L_3, L_2, and L_1 absorption edges overlap. Unless these overlapping contributions are disentangled, extracting structural information from the data via traditional data analysis strategies is either not possible [149, 150] or difficult and/or insufficiently accurate [151].

The problem of overlapping edges in EXAFS analysis is not limited to heterometallic catalysts, of course. $BaTiO_3$ is among the most extensively studied perovskites, yet its EXAFS studies are complicated due to the overlap of Ti K-edge and Ba L_3 edge. B. Ravel et al. proposed a very original use of diffraction

anomalous fine structure (DAFS) technique to deconvolute the EXAFS signals from Ti and Ba [152, 153]. Other methods have appeared recently, based on the use of the high energy resolution fluorescence detection (HERFD) that enabled separation of emission lines from different elements [85, 154–156].

Menard et al. reported a new method for deconvolution of overlapping absorption edges that is based on the use of concurrent, multiple edge analysis of EXAFS data from each edge [63]. The analysis strategy is demonstrated here for an arbitrary bimetallic composition even though, for illustration purpose only, they used notation Ir and Pt for its constituent elements. Data analysis is done by a simultaneous fit of both Ir L_3 and Pt L_3 edges, which involve three contributions: (1) the Ir EXAFS in the Ir L_3 edge before the Pt L_3 edge; (2) the Ir EXAFS in the Pt L_3 edge; and (3) the Pt EXAFS in the Pt L_3 edge. Because (1) and (2) describe the same coordination environments they should be constrained analytically, in the process of fitting each contribution to the experimental data. The analysis is done in r-space and is limited to nearest neighbor scattering paths, which are usually well isolated from longer scattering paths in the Fourier transforms of the EXAFS signal $\chi(k)$. In this case, the EXAFS equations that are simultaneously fit are:

$$\chi_{\text{Ir edge}}(k_{\text{Ir}}) = \frac{S_{0,\text{Ir}}^2 N_{\text{Ir}}}{k_{\text{Ir}} R_{\text{Ir}}^2} \left| f_{\text{Ir}}^{eff}(k_{\text{Ir}}) \right| \sin\left[2k_{\text{Ir}} R_{\text{Ir}} - \frac{4}{3}\sigma_{\text{Ir}}^{(3)} k_{\text{Ir}}^3 + \delta_{\text{Ir}}(k_{\text{Ir}}) \right] e^{-2\sigma_{\text{Ir}}^2 k_{\text{Ir}}^2} e^{-2R_{\text{Ir}}/\lambda_{\text{Ir}}(k_{\text{Ir}})}, \tag{19.17}$$

and

$$\begin{aligned} \chi_{\text{Pt edge}}(k_{\text{Pt}}, k_{\text{Ir}}) = {} & \frac{S_{0,\text{Pt}}^2 N_{\text{Pt}}}{k_{\text{Pt}} R_{\text{Pt}}^2} \left| f_{\text{Pt}}^{eff}(k_{\text{Pt}}) \right| \sin\left[2k_{\text{Pt}} R_{\text{Pt}} - \frac{4}{3}\sigma_{\text{Pt}}^{(3)} k_{\text{Pt}}^3 + \delta_{\text{Pt}}(k_{\text{Pt}}) \right] \\ & \times e^{-2\sigma_{\text{Pt}}^2 k_{\text{Pt}}^2} e^{-2R_{\text{Pt}}/\lambda_{\text{Pt}}(k_{\text{Pt}})} + \frac{A S_{0,\text{Ir}}^2 N_{\text{Ir}}}{k_{\text{Ir}} R_{\text{Ir}}^2} \left| f_{\text{Ir}}^{eff}(k_{\text{Ir}}) \right| \sin \\ & \times \left[2k_{\text{Ir}} R_{\text{Ir}} - \frac{4}{3}\sigma_{\text{Ir}}^{(3)} k_{\text{Ir}}^3 + \delta_{\text{Ir}}(k_{\text{Ir}}) \right] e^{-2\sigma_{\text{Ir}}^2 k_{\text{Ir}}^2} e^{-2R_{\text{Ir}}/\lambda_{\text{Ir}}(k_{\text{Ir}})}. \end{aligned} \tag{19.18}$$

The factor $A = \Delta\mu_{0,\text{Ir}}/\Delta\mu_{0,\text{Pt}}$, where $\Delta\mu_{0,\text{Ir}}$ and $\Delta\mu_{0,\text{Pt}}$ are the changes in the absorption at the edge steps, is necessary because the extraction of $\chi(k)$ includes a normalization to these edge steps. The nonlinear least squares fitting of experimental data to Eqs. (19.17 and 19.18) should be done concurrently to the overlapping L_3 edges and can be achieved using available EXAFS analysis tools. In ref. [63], the interface programs Athena and Artemis were used. In practice, correction of the energy grid in k-space for the Ir EXAFS in the Pt L_3 edge should be made. The correction to the threshold energy (in eV) for the Ir EXAFS in the Pt L_3 edge is defined as $\Delta E_{0,\text{Ir}} - (349 + \Delta E_{0,\text{Pt}})$, where 349 eV is the difference between the empirical threshold energies. Such a large energy origin shift is necessary in this method since it accounts for a unique $k = 0$ reference point for the Ir EXAFS extending beyond the Pt edge when the Pt edge EXAFS is transformed to k-

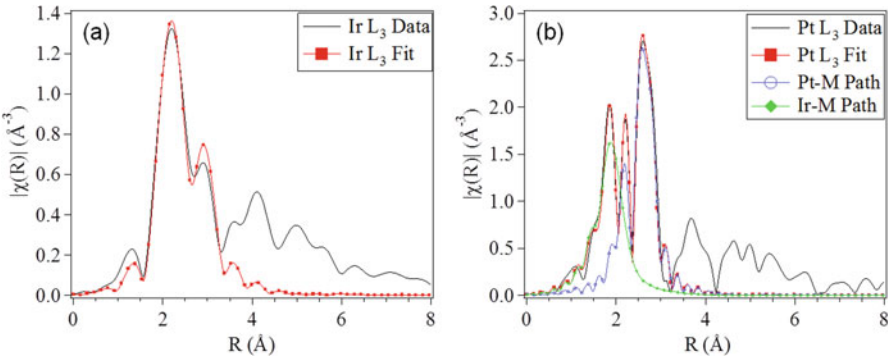

Fig. 19.7 Comparison of the data and fit of the Ir-Pt NPs on γ-Al_2O_3 under a H_2 atm measured at 215 K at the Ir L_3 and Pt L_3 absorption edges. Fourier transform magnitude of (**a**) the Ir L_3 data and fit, and (**b**) the Pt L_3 data and fit with the contributions of the individual paths represented. Reproduced with permission from ref. [63]

space. The exact value to use (here 349 eV) will depend on the E_0 values that are used in the edge subtraction of the EXAFS spectra. The representative data and fits in r-space are shown in Fig. 19.7. The signature of the Ir L_3 EXAFS "leaking" into the Pt L_3 EXAFS is a low r feature in Fig. 19.7b.

19.8 Outlook and Future Developments

With the ongoing development of X-ray absorption spectroscopy techniques, the opportunities for investigation of mechanisms of catalytic reactions employing nanoscale metal catalysts are growing and new challenges, previously ignored or overlooked, come to the surface. One such important challenge is the heterogeneity of the NP ensembles that is evident even in samples with narrow size and compositional distributions and is a common property of real catalysts with large compositional gradients. That heterogeneity, when ignored, causes artifacts in data analysis, as demonstrated above in the case of the compositional heterogeneity, and is also shown by Yevick and Frenkel [109] for the case of the structural heterogeneity due to surface relaxation in nm-scale clusters.

One possible solution is the single nanoparticle spectroscopy studies by XAS methods [157]. Current and future capabilities of X-ray spectromicroscopy based on coherence-limited imaging methods including nano-probe methods were discussed by Hitchcock and Toney [158]. These methods will benefit from the dramatic increase in brightness expected from a diffraction-limited storage ring. The applicability of nano-probe methods for spectroscopy studies of single NPs was illustrated by Y. Chu's group. They studied the oxidation process of individual PtNi NPs by a scanning multilayer Laue lens X-ray microscope and discovered the transformation of alloyed PtNi (140 to 320 nm) to Pt/NiO core–shell and the further

coalescence under thermal oxidation [159]. The scanning was performed using 10 nm step size and 30 nm focal spot size at beamline 26ID of the Advanced Photon Source at Argonne National Laboratory. This method is being developed for to the hard X-ray nanoprobe (HXN) beamline of the National Synchrotron Light Source II at BNL. Alternatively, photoemission electron microscopy was used for studying of individual Co NPs with the size of 8 nm. Significant variations in the shapes of the Co $L_{2,3}$ edges of the X-ray absorption spectra between different cobalt NPs were detected and attributed to different cobalt–oxygen interactions on a particle-by-particle basis [160]. For these spectromicroscopic methods on the basis of nanoprobe, the main challenge is to keep high flux while reducing the spot size. More details on challenges and limitations of nano-probe methods for catalytic investigations were addressed recently by Frenkel and van Bokhoven [157].

Studying nanocatalysts at the single-nanoparticle level and in *operando* mode adds more challenges. For spectroscopic methods, the key is to increase particle sensitivity and for electron microscopic methods it's to enable realistic working conditions. In most electron microscopy studies of catalysis, they were either investigated in an ex-situ mode, i.e., catalysts were pretreated elsewhere under controlled conditions of atmosphere, pressure and temperature, while measured under high vacuum at low temperatures, or under simulated working conditions with lower temperature and pressure compared to the real ones [46, 161, 162]. To bridge this "pressure gap", a new mode of operation is needed, where relevant (for structural analysis) techniques can probe catalysts in the same reaction conditions. Recently, Stach and Frenkel demonstrated the advantage of using such a micro-reactor, for nanocatalysis studies at ambient temperature and pressure [104]. Basing on the idea of combining electron microscopy with spectroscopic techniques by sharing the same reactor to make sure samples/conditions under study are the same for all types of techniques [163, 164], the group discovered the complex structural dynamics of Pt/SiO_2 under ethylene hydrogenation conditions that occurs at broad length scale [104].

In conclusion, with the development of XAFS instrumentation and analysis methods, the understanding of structure of nanoparticle catalysts is advanced from qualitative pictures of the mid-70s to much more quantitative ones that are capable to capture fine architectural and compositional details, and account for interparticle and intraparticle heterogeneities. More achievements are expected in the coming years, owing to the reduced beam sizes, improved energy and time resolutions, and new developments in the combinations of XAFS with complementary imaging and scattering methods in *operando* conditions.

References

1. Gilbert B, Huang F, Zhang H et al (2004) Nanoparticles: strained and stiff. Science 305:651–654
2. Zobel M, Neder RB, Kimber SAJ (2015) Universal solvent restructuring induced by colloidal nanoparticles. Science 347:292–294
3. Dreaden EC, Alkilany AM, Huang X et al (2012) The golden age: gold nanoparticles for biomedicine. Chem Soc Rev 41:2740–2779

4. Xu B, Zhang ZC, Wang X (2014) Engineering nanointerfaces for nanocatalysis. Chem Soc Rev 43:7870–7886
5. Sanchez SI, Menard LD, Bram A et al (2009) The emergence of nonbulk properties in supported metal clusters: negative thermal expansion and atomic disorder in Pt nanoclusters supported on γ-Al_2O_3. J Am Chem Soc 131:7040–7054
6. Mostafa S, Behafarid F, Croy JR et al (2010) Shape-dependent catalytic properties of Pt nanoparticles. J Am Chem Soc 132:15714–15719
7. Crespo-Quesada M, Yarulin A, Jin M et al (2011) Structure sensitivity of alkynol hydrogenation on shape- and size-controlled palladium nanocrystals: which sites are most active and selective? J Am Chem Soc 133:12787–12794
8. Jaramillo TF, Jørgensen KP, Bonde J et al (2007) Identification of active edge sites for electrochemical H_2 evolution from MoS_2 nanocatalysts. Science 317:100–102
9. Yudanov IV, Sahnoun R, Neyman KM et al (2002) CO adsorption on Pd nanoparticles: density functional and vibrational spectroscopy studies. J Phys Chem B 107:255–264
10. Walsh MJ, Yoshida K, Kuwabara A et al (2012) On the structural origin of the catalytic properties of inherently strained ultrasmall decahedral gold nanoparticles. Nano Lett 12:2027–2031
11. Ruban A, Hammer B, Stoltze P et al (1997) Surface electronic structure and reactivity of transition and noble metals. J Mol Catal A: Chem 115:421–429
12. Small MW, Kas JJ, Kvashnina KO et al (2014) Effects of adsorbate coverage and bond-length disorder on the d-band center of carbon-supported Pt catalysts. ChemPhysChem 15:1569–1572
13. Norskov JK, Bligaard T, Rossmeisl J et al (2009) Towards the computational design of solid catalysts. Nat Chem 1:37–46
14. Nørskov JK, Abild-Pedersen F, Studt F et al (2011) Density functional theory in surface chemistry and catalysis. Proc Natl Acad Sci U S A 108:937–943
15. Stamenkovic VR, Mun BS, Arenz M et al (2007) Trends in electrocatalysis on extended and nanoscale Pt-bimetallic alloy surfaces. Nat Mater 6:241–247
16. Huang WJ, Sun R, Tao J et al (2008) Coordination-dependent surface atomic contraction in nanocrystals revealed by coherent diffraction. Nat Mater 7:308–313
17. Ouyang G, Zhu WG, Sun CQ et al (2010) Atomistic origin of lattice strain on stiffness of nanoparticles. Phys Chem Chem Phys 12:1543–1549
18. Li L, Wang L-L, Johnson DD et al (2013) Noncrystalline-to-crystalline transformations in Pt nanoparticles. J Am Chem Soc 135:13062–13072
19. Frenkel AI, Small MW, Smith JG et al (2013) An in situ study of bond strains in 1 nm Pt catalysts and their sensitivities to cluster–support and cluster–adsorbate interactions. J Phys Chem C 117:23286–23294
20. Vermaak JS, Mays CW, Kuhlmann D (1968) On surface stress and surface tension.I. Theoretical considerations. Surf Sci 12:128–133
21. Frenkel AI, Nemzer S, Pister I et al (2005) Size-controlled synthesis and characterization of thiol-stabilized gold nanoparticles. J Chem Phys 123:184701–184706
22. Roldan Cuenya B, Frenkel AI, Mostafa S et al (2010) Anomalous lattice dynamics and thermal properties of supported size- and shape-selected Pt nanoparticles. Phys Rev B 82:155450
23. Sanchez SI, Small MW, J-M Z et al (2009) Structural characterization of Pt − Pd and Pd − Pt core − shell nanoclusters at atomic resolution. J Am Chem Soc 131:8683–8689
24. Frenkel AI, Machavariani VS, Rubshtein A et al (2000) Local structure of disordered Au-Cu and Au-Ag alloys. Phys Rev B 62:9364–9371
25. Frenkel AI, Stern EA, Voronel A et al (1996) Lattice strains in disordered mixed salts. Solid State Commun 99:67–71
26. Kibler LA, El-Aziz AM, Hoyer R et al (2005) Tuning reaction rates by lateral strain in a palladium monolayer. Angew Chem Int Ed 44:2080–2084

27. Kitchin JR, Nørskov JK, Barteau MA et al (2004) Role of strain and ligand effects in the modification of the electronic and chemical properties of bimetallic surfaces. Phys Rev Lett 93:156801
28. Mavrikakis M, Hammer B, Nørskov JK (1998) Effect of strain on the reactivity of metal surfaces. Phys Rev Lett 81:2819–2822
29. Sun CQ (2007) Size dependence of nanostructures: impact of bond order deficiency. Prog Solid State Chem 35:1–159
30. Hammer B, Nørskov JK (2000) Theoretical surface science and catalysis—calculations and concepts. In: Knozinger H, Gates BC (eds) Advances in catalysis. Academic, New York, pp 71–129
31. Kitchin JR, Nørskov JK, Barteau MA et al (2004) Modification of the surface electronic and chemical properties of Pt(111) by subsurface 3d transition metals. J Chem Phys 120:10240–10246
32. Comotti M, Li W-C, Spliethoff B et al (2005) Support effect in high activity gold catalysts for CO oxidation. J Am Chem Soc 128:917–924
33. Graoui H, Giorgio S, Enry CR (2001) Effect of the interface structure on the high-temperature morphology of supported metal clusters. Philos Mag B 81:1649–1658
34. Campbell CT, Sharp JC, Yao YX et al (2011) Insights into catalysis by gold nanoparticles and their support effects through surface science studies of model catalysts. Faraday Discuss 152:227–239
35. Campbell CT, Sellers JRV (2013) Anchored metal nanoparticles: effects of support and size on their energy, sintering resistance and reactivity. Faraday Discuss 162:9–30
36. Xu R, Wang D, Zhang J et al (2006) Shape-dependent catalytic activity of silver nanoparticles for the oxidation of styrene. Chem Asian J 1:888–893
37. Tian N, Zhou Z-Y, Sun S-G et al (2007) Synthesis of tetrahexahedral platinum nanocrystals with high-index facets and high electro-oxidation activity. Science 316:732–735
38. Karim AM, Prasad V, Mpourmpakis G et al (2009) Correlating particle size and shape of supported Ru/γ-Al_2O_3 catalysts with NH_3 decomposition activity. J Am Chem Soc 131:12230–12239
39. Häkkinen H, Abbet S, Sanchez A et al (2003) Structural, electronic, and impurity-doping effects in nanoscale chemistry: supported gold nanoclusters. Angew Chem Int Ed 42:1297–1300
40. Kacprzak KA, Akola J, Hakkinen H (2009) First-principles simulations of hydrogen peroxide formation catalyzed by small neutral gold clusters. Phys Chem Chem Phys 11:6359–6364
41. Ferrando R, Jellinek J, Johnston RL (2008) Nanoalloys: from theory to applications of alloy clusters and nanoparticles. Chem Rev 108:845–910
42. Ghosh Chaudhuri R, Paria S (2012) Core/shell nanoparticles: classes, properties, synthesis mechanisms, characterization, and applications. Chem Rev 112:2373–2433
43. Tupy SA, Karim AM, Bagia C et al (2012) Correlating ethylene glycol reforming activity with in situ EXAFS detection of Ni segregation in supported NiPt bimetallic catalysts. ACS Catal 2:2290–2296
44. Alayoglu S, Tao F, Altoe V et al (2011) Surface composition and catalytic evolution of $Au_x Pd_{1-x}$ ($x = 0.25$, 0.50 and 0.75) nanoparticles under CO/O_2 reaction in Torr pressure regime and at 200 °C. Catal Lett 141:633–640
45. Alayoglu S, Zavalij P, Eichhorn B et al (2009) Structural and architectural evaluation of bimetallic nanoparticles: a case study of Pt − Ru core − shell and alloy nanoparticles. ACS Nano 3:3127–3137
46. Yoshida H, Kuwauchi Y, Jinschek JR et al (2012) Visualizing gas molecules interacting with supported nanoparticulate catalysts at reaction conditions. Science 335:317–319
47. Adriano F (2001) EXAFS for liquids. J Phys Condens Matter 13:R23
48. Sharpe LR, Heineman WR, Elder RC (1990) EXAFS spectroelectrochemistry. Chem Rev 90:705–722

49. Russell AE, Rose A (2004) X-ray absorption spectroscopy of low temperature fuel cell catalysts. Chem Rev 104:4613–4636
50. Bentrup U (2010) Combining in situ characterization methods in one set-up: looking with more eyes into the intricate chemistry of the synthesis and working of heterogeneous catalysts. Chem Soc Rev 39:4718–4730
51. Comez L, Di Cicco A, Itié JP et al (2001) High-pressure and high-temperature X-ray absorption study of liquid and solid gallium. Phys Rev B 65:014114
52. Vankó G, Rueff J-P, Mattila A et al (2006) Temperature- and pressure-induced spin-state transitions in $LaCoO_3$. Phys Rev B 73:024424
53. Meunier FC (2010) The design and testing of kinetically-appropriate operando spectroscopic cells for investigating heterogeneous catalytic reactions. Chem Soc Rev 39:4602–4614
54. Bare SR, Yang N, Kelly SD et al (2007) Design and operation of a high pressure reaction cell for in situ X-ray absorption spectroscopy. Catal Today 126:18–26
55. Bare SR, Mickelson GE, Modica FS et al (2006) Simple flow through reaction cells for in situ transmission and fluorescence X-ray-absorption spectroscopy of heterogeneous catalysts. Rev Sci Instrum 77:023105
56. Grunwaldt JD, Caravati M, Hannemann S et al (2004) X-ray absorption spectroscopy under reaction conditions: suitability of different reaction cells for combined catalyst characterization and time-resolved studies. Phys Chem Chem Phys 6:3037–3047
57. Grunwaldt J-D, Ramin M, Rohr M et al (2005) High pressure in situ X-ray absorption spectroscopy cell for studying simultaneously the liquid phase and the solid/liquid interface. Rev Sci Instrum 76:054104
58. Erickson EM, Oruc ME, Wetzel DJ et al (2014) A comparison of atomistic and continuum approaches to the study of bonding dynamics in electrocatalysis: microcantilever stress and in situ EXAFS observations of platinum bond expansion due to oxygen adsorption during the oxygen reduction reaction. Anal Chem 86:8368–8375
59. Glasner D, Frenkel AI (2007) Geometrical characteristics of regular polyhedra: application to EXAFS studies of nanoclusters. AIP Conf Proc 882:746–748
60. Frenkel AI (2007) Solving the 3D structure of metal nanoparticles. Z Kristallogr 222:605–611
61. Small MW, Sanchez SI, Marinkovic NS et al (2012) Influence of adsorbates on the electronic structure, bond strain, and thermal properties of an alumina-supported Pt catalyst. ACS Nano 6:5583–5595
62. Frenkel AI, Wang Q, Sanchez SI et al (2013) Short range order in bimetallic nanoalloys: an extended X-ray absorption fine structure study. J Chem Phys 138:064202
63. Menard LD, Wang Q, Kang JH et al (2009) Structural characterization of bimetallic nanomaterials with overlapping X-ray absorption edges. Phys Rev B 80:064111
64. Funke H, Scheinost AC, Chukalina M (2005) Wavelet analysis of extended X-ray absorption fine structure data. Phys Rev B 71:094110
65. Chukalina MV, Dubrovskii YV, Funke H (2004) Wavelet analysis and its application in tunneling and X-ray spectroscopy. Low Temp Phys 30:930–936
66. Filez M, Redekop EA, Poelman H et al (2015) Advanced elemental characterization during Pt–In catalyst formation by wavelet transformed X-ray absorption spectroscopy. Anal Chem 87:3520–3526
67. Filez M, Redekop EA, Poelman H et al (2014) Unravelling the formation of Pt–Ga alloyed nanoparticles on calcined Ga-modified hydrotalcites by in situ XAS. Chem Mater 26:5936–5949
68. Antoniak C (2011) Extended X-ray absorption fine structure of bimetallic nanoparticles. Beilstein J Nanotechnol 2:237–251
69. Ferri D, Kumar MS, Wirz R et al (2010) First steps in combining modulation excitation spectroscopy with synchronous dispersive EXAFS/DRIFTS/mass spectrometry for in situ time resolved study of heterogeneous catalysts. Phys Chem Chem Phys 12:5634–5646

70. Eyssler A, Kleymenov E, Kupferschmid A et al (2011) Improvement of catalytic activity of $LaFe_{0.95}Pd_{0.05}O_3$ for methane oxidation under transient conditions. J Phys Chem C 115:1231–1239
71. Ferri D, Newton MA, Di Michiel M et al (2013) Synchrotron high energy X-ray methods coupled to phase sensitive analysis to characterize aging of solid catalysts with enhanced sensitivity. Phys Chem Chem Phys 15:8629–8639
72. König CFJ, van Bokhoven JA, Schildhauer TJ et al (2012) Quantitative analysis of modulated excitation X-ray absorption spectra: enhanced precision of EXAFS fitting. J Phys Chem C 116:19857–19866
73. König CFJ, Schildhauer TJ, Nachtegaal M (2013) Methane synthesis and sulfur removal over a Ru catalyst probed in situ with high sensitivity X-ray absorption spectroscopy. J Catal 305:92–100
74. Patlolla A, Baumann P, Xu W et al (2013) Characterization of metal-oxide catalysts in operando conditions by combining X-ray absorption and raman spectroscopies in the same experiment. Top Catal 56:896–904
75. Frenkel AI, Wang Q, Marinkovic N et al (2011) Combining X-ray absorption and X-ray diffraction techniques for in situ studies of chemical transformations in heterogeneous catalysis: advantages and limitations. J Phys Chem C 115:17884–17890
76. Patlolla A, Carino EV, Ehrlich SN et al (2012) Application of operando XAS, XRD, and Raman spectroscopy for phase speciation in water gas shift reaction catalysts. ACS Catal 2:2216–2223
77. Chen Y, Fulton JL, Linehan JC et al (2005) In situ XAFS and NMR study of rhodium-catalyzed dehydrogenation of dimethylamine borane. J Am Chem Soc 127:3254–3255
78. Beale AM, van der Eerden AMJ, Kervinen K et al (2005) Adding a third dimension to operando spectroscopy: a combined UV-Vis, Raman and XAFS setup to study heterogeneous catalysts under working conditions. Chem Commun 3015–3017
79. Newton MA, Jyoti B, Dent AJ et al (2004) Synchronous, time resolved, diffuse reflectance FT-IR, energy dispersive EXAFS (EDE) and mass spectrometric investigation of the behaviour of Rh catalysts during NO reduction by CO. Chem Commun 2382–2383
80. Bordiga S, Groppo E, Agostini G et al (2013) Reactivity of surface species in heterogeneous catalysts probed by in situ X-ray absorption techniques. Chem Rev 113:1736–1850
81. Singh J, Lamberti C, van Bokhoven JA (2010) Advanced X-ray absorption and emission spectroscopy: in situ catalytic studies. Chem Soc Rev 39:4754–4766
82. van Bokhoven JA, Louis C, Miller JT et al (2006) Activation of oxygen on gold/alumina catalysts: in situ high-energy-resolution fluorescence and time-resolved X-ray spectroscopy. Angew Chem 118:4767–4770
83. Tromp M, van Bokhoven JA, Safonova OV et al (2007) High energy resolution fluorescence detection X-ray absorption spectroscopy: detection of adsorption sites in supported metal catalysts. AIP Conf Proc 882:651–653
84. Glatzel P, Singh J, Kvashnina KO et al (2010) In situ characterization of the 5d density of states of Pt nanoparticles upon adsorption of CO. J Am Chem Soc 132:2555–2557
85. Hübner M, Koziej D, Bauer M et al (2011) The structure and behavior of platinum in SnO_2-based sensors under working conditions. Angew Chem Int Ed 50:2841–2844
86. Oudenhuijzen MK, van Bokhoven JA, Miller JT et al (2005) Three-site model for hydrogen adsorption on supported platinum particles: influence of support ionicity and particle size on the hydrogen coverage. J Am Chem Soc 127:1530–1540
87. Tromp M, Slagt MQ, Klein Gebbink RJM et al (2004) Atomic XAFS as a probe of electron transfer within organometallic complexes: data analysis and theoretical calculations. Phys Chem Chem Phys 6:4397–4406
88. Porosoff MD, Yu W, Chen JG (2013) Challenges and opportunities in correlating bimetallic model surfaces and supported catalysts. J Catal 308:2–10
89. Evans J (1989) EXAFS in the study of catalysts. In: Bond GC, Webb G (ed) Catalysis: volume 8, The Royal Society of Chemistry, p 1–41

90. Sayers DE, Stern EA, Lytle FW (1971) New technique for investigating noncrystalline structures: Fourier analysis of the extended X-ray-absorption fine structure. Phys Rev Lett 27:1204–1207
91. Stern EA (1974) Theory of the extended X-ray-absorption fine structure. Phys Rev B 10:3027–3037
92. Lytle FW, Sayers DE, Stern EA (1975) Extended X-ray-absorption fine-structure technique. II. Experimental practice and selected results. Phys Rev B 11:4825–4835
93. Stern EA, Sayers DE, Lytle FW (1975) Extended X-ray-absorption fine-structure technique. III. Determination of physical parameters. Phys Rev B 11:4836–4846
94. Lee PA, Pendry JB (1975) Theory of the extended X-ray absorption fine structure. Phys Rev B 11:2795–2811
95. Sinfelt JH, Via GH, Lytle FW (1978) Extended X-ray absorption fine structure (EXAFS) of supported platinum catalysts. J Chem Phys 68:2009–2010
96. Via GH, Sinfelt JH, Lytle FW (1979) Extended X-ray absorption fine structure (EXAFS) of dispersed metal catalysts. J Chem Phys 71:690–699
97. Sinfelt JH, Via GH, Lytle FW (1980) Structure of bimetallic clusters. Extended X-ray absorption fine structure (EXAFS) studies of Ru–Cu clusters. J Chem Phys 72:4832–4844
98. Via GH, Sinfelt JH, Lytle FW (1981) EXAFS studies of supported metal catalysts. In: Joy DC, Teo BK (eds) EXAFS spectroscopy. Springer, New York, pp 159–162
99. Mustre J, Yacoby Y, Stern EA et al (1990) Analysis of experimental extended X-ray-absorption fine-structure (EXAFS) data using calculated curved-wave, multiple-scattering EXAFS spectra. Phys Rev B 42:10843–10851
100. Frenkel AI, Yevick A, Cooper C et al (2011) Modeling the structure and composition of nanoparticles by extended X-ray absorption fine-structure spectroscopy. Annu Rev Anal Chem 4:23–39
101. Calvin S, Miller MM, Goswami R et al (2003) Determination of crystallite size in a magnetic nanocomposite using extended X-ray absorption fine structure. J Appl Phys 94:778–783
102. Montejano-Carrizales JM, Aguilera-Granja F, Morán-López JL (1997) Direct enumeration of the geometrical characteristics of clusters. Nanostruct Mater 8:269–287
103. Montejano-Carrizales JM, Morán-López JL (1992) Geometrical characteristics of compact nanoclusters. Nanostruct Mater 1:397–409
104. Li Y, Zakharov D, Zhao S et al (2015) Complex structural dynamics of nanocatalysts revealed in operando conditions by correlated imaging and spectroscopy probes. Nat Commun
105. Frenkel AI, Frankel SC, Liu T (2005) Structural stability of giant polyoxomolybdate molecules as probed by EXAFS. Phys Sci 2005:721
106. Frenkel AI, Hills CW, Nuzzo RG (2001) A view from the inside: complexity in the atomic scale ordering of supported metal nanoparticles. J Phys Chem B 105:12689–12703
107. Roldan Cuenya B, Croy JR, Mostafa S et al (2010) Solving the structure of size-selected Pt nanocatalysts synthesized by inverse micelle encapsulation. J Am Chem Soc 132:8747–8756
108. Stern EA (1988) Theory of EXAFS. In: Koningsberger DC, Prins R (eds) X-ray absorption: principles, applications, techniques of EXAFS, SEXAFS, and XANES. John Wiley & Sons, New York
109. Yevick A, Frenkel AI (2010) Effects of surface disorder on EXAFS modeling of metallic clusters. Phys Rev B 81:115451
110. Chill ST, Anderson RM, Yancey DF et al (2015) Probing the limits of conventional extended X-ray absorption fine structure analysis using thiolated gold nanoparticles. ACS Nano 9:4036–4042
111. Roscioni OM, Zonias N, Price SWT et al (2011) Computational prediction of L_3 EXAFS spectra of gold nanoparticles from classical molecular dynamics simulations. Phys Rev B 83:115409
112. Vila F, Rehr JJ, Kas J et al (2008) Dynamic structure in supported Pt nanoclusters: real-time density functional theory and X-ray spectroscopy simulations. Phys Rev B 78:121404

113. Frenkel A, Yang J, Johnson D et al (2009) Nanoscale atomic clusters, complexity of. In: Meyers RA (ed) Encyclopedia of complexity and systems science. Springer, New York, pp 5889–5912
114. Frenkel AI (1999) Solving the structure of nanoparticles by multiple-scattering EXAFS analysis. J Synchrotron Radiat 6:293–295
115. Frenkel AI, Cason MW, Elsen A et al (2014) Critical review: effects of complex interactions on structure and dynamics of supported metal catalysts. J Vac Sci Technol A 32:020801
116. Matos J, Ono LK, Behafarid F et al (2012) In situ coarsening study of inverse micelle-prepared Pt nanoparticles supported on γ-Al_2O_3: pretreatment and environmental effects. Phys Chem Chem Phys 14:11457–11467
117. Paredis K, Ono LK, Mostafa S et al (2011) Structure, chemical composition, and reactivity correlations during the in situ oxidation of 2-Propanol. J Am Chem Soc 133:6728–6735
118. Munoz-Paez A, Koningsberger DC (1995) Decomposition of the precursor $[Pt(NH_3)_4](OH)_2$, genesis and structure of the metal-support interface of alumina supported platinum particles: a structural study using TPR, MS, and XAFS spectroscopy. J Phys Chem 99:4193–4204
119. Giovanetti LJ, Ramallo-López JM, Foxe M et al (2012) Shape changes of Pt nanoparticles induced by deposition on mesoporous silica. Small 8:468–473
120. Vaarkamp M, Miller JT, Modica FS et al (1996) On the relation between particle morphology, structure of the metal-support interface, and catalytic properties of Pt/γ-Al_2O_3. J Catal 163:294–305
121. Vaarkamp M, Modica FS, Miller JT et al (1993) Influence of hydrogen pretreatment on the structure of the metal-support interface in Pt/zeolite catalysts. J Catal 144:611–626
122. Jentys A (1999) Estimation of mean size and shape of small metal particles by EXAFS. Phys Chem Chem Phys 1:4059–4063
123. Beale AM, Weckhuysen BM (2010) EXAFS as a tool to interrogate the size and shape of mono and bimetallic catalyst nanoparticles. Phys Chem Chem Phys 12:5562–5574
124. Long NV, Asaka T, Matsubara T et al (2011) Shape-controlled synthesis of Pt–Pd core–shell nanoparticles exhibiting polyhedral morphologies by modified polyol method. Acta Mater 59:2901–2907
125. Long NV, Duy Hien T, Asaka T et al (2011) Synthesis and characterization of Pt–Pd alloy and core-shell bimetallic nanoparticles for direct methanol fuel cells (DMFCs): Enhanced electrocatalytic properties of well-shaped core-shell morphologies and nanostructures. Int J Hydr Energ 36:8478–8491
126. Anderson JA, Garcia MF (eds) (2005) Supported metals in catalysis. Imperial College Press, London
127. Guczi L (2005) Bimetallic nano-particles: featuring structure and reactivity. Catal Today 101:53–64
128. Bukhtiyarov VG, Slin'ko M (2001) Metallic nanosystems in catalysis. Russ Chem Rev 70:147–159
129. Bazin D, Mottet C, Tréglia G (2000) New opportunities to understand heterogeneous catalysis processes on nanoscale bimetallic particles through synchrotron radiation and theoretical studies. Appl Catal A: Gen 200:47–54
130. Rase HF (2000) Handbook of commercial catalysts: heterogeneous catalysts. CRC Press, Boca Raton
131. Yang OB, Woo SI, Kim YG (1994) Comparison of platinum-iridium bimetallic catalysts supported on γ-alumina and HY-zeolite in n-hexane reforming reaction. Appl Catal A: Gen 115:229–241
132. Nashner MS, Frenkel AI, Adler DL et al (1997) Structural characterization of carbon-supported platinum – ruthenium nanoparticles from the molecular cluster precursor $PtRu_5C(CO)_{16}$. J Am Chem Soc 119:7760–7771
133. Nashner MS, Frenkel AI, Somerville D et al (1998) Core shell inversion during nucleation and growth of bimetallic Pt/Ru nanoparticles. J Am Chem Soc 120:8093–8101

134. Hills CW, Nashner MS, Frenkel AI et al (1999) Carbon support effects on bimetallic Pt – Ru nanoparticles formed from molecular precursors. Langmuir 15:690–700
135. Knecht MR, Weir MG, Frenkel AI et al (2007) Structural rearrangement of bimetallic alloy PdAu nanoparticles within dendrimer templates to yield core/shell configurations. Chem Mater 20:1019–1028
136. Weir MG, Knecht MR, Frenkel AI et al (2009) Structural analysis of PdAu dendrimer-encapsulated bimetallic nanoparticles. Langmuir 26:1137–1146
137. Toshima N, Harada M, Yonezawa T et al (1991) Structural analysis of polymer-protected palladium/platinum bimetallic clusters as dispersed catalysts by using extended X-ray absorption fine structure spectroscopy. J Phys Chem 95:7448–7453
138. Toshima N, Yonezawa T (1998) Bimetallic nanoparticles-novel materials for chemical and physical applications. New J Chem 22:1179–1201
139. Asakura K, Bian CR, Suzuki S et al (2005) An XAFS study on the polymer protected CuPd bimetallic nanoparticles – a novel heterobond-philic structure. Phys Sci T115:781
140. Harada M, Asakura K, Toshima N (1994) Structural analysis of polymer-protected platinum/rhodium bimetallic clusters using extended X-ray absorption fine structure spectroscopy. Importance of microclusters for the formation of bimetallic clusters. J Phys Chem 98:2653–2662
141. Kulkarni UD, Banerjee S, Krishnan RV (1985) On clustering and ordering instabilities in FCC solid solutions. Mater Sci Forum 3:111–121
142. Ma E (2005) Alloys created between immiscible elements. Prog Mater Sci 50:413–509
143. Cowley JM (1950) An approximate theory of order in alloys. Phys Rev 77:669–675
144. Cowley JM (1960) Short- and long-range order parameters in disordered solid solutions. Phys Rev 120:1648–1657
145. Cowley JM (1965) Short-range order and long-range order parameters. Phys Rev 138: A1384–A1389
146. Agostini G, Pellegrini R, Leofanti G et al (2009) Determination of the particle size, available surface area, and nature of exposed sites for silica-alumina-supported Pd nanoparticles: a multitechnical approach. J Phys Chem C 113:10485–10492
147. Hwang B-J, Sarma LS, Chen J-M et al (2005) Structural models and atomic distribution of bimetallic nanoparticles as investigated by X-ray absorption spectroscopy. J Am Chem Soc 127:11140–11145
148. Frenkel AI (2012) Applications of extended X-ray absorption fine-structure spectroscopy to studies of bimetallic nanoparticle catalysts. Chem Soc Rev 41:8163–8178
149. Flavell WR, Mian M, Roberts AJ et al (1997) EXAFS studies of $SrSn_{1-x}Sb_xO_3$ and $BaPb_{1-x}Bi_xO_3$. J Mater Chem 7:357–364
150. Michel CG, Bambrick WE, Ebel RH et al (1995) Reducibility of rhenium in Pt-Re/Al_2O_3 reforming catalysts: a temperature programmed reduction-X-ray-absorption near-edge structure study. J Catal 154:222–229
151. Rønning M, Gjervan T, Prestvik R et al (2001) Influence of pretreatment temperature on the bimetallic interactions in Pt-Re/Al_2O_3 reforming catalysts studied by X-ray absorption spectroscopy. J Catal 204:292–304
152. Ravel B, Bouldin CE, Renevier H et al (1999) Edge separation using diffraction anomalous fine structure. J Synchrotron Radiat 6:338–340
153. Ravel B, Bouldin CE, Renevier H et al (1999) X-ray-absorption edge separation using diffraction anomalous fine structure. Phys Rev B 60:778–785
154. Glatzel P, de Groot FMF, Manoilova O et al (2005) Range-extended EXAFS at the *L* edge of rare earths using high-energy-resolution fluorescence detection: A study of La in LaOCl. Phys Rev B 72:014117
155. Yano J, Pushkar Y, Glatzel P et al (2005) High-resolution Mn EXAFS of the oxygen-evolving complex in photosystem II: structural implications for the Mn4Ca cluster. J Am Chem Soc 127:14974–14975

156. Pushkar Y, Yano J, Glatzel P et al (2007) Structure and orientation of the Mn_4Ca cluster in plant photosystem II membranes studied by polarized range-extended X-ray absorption spectroscopy. J Biol Chem 282:7198–7208
157. Frenkel AI, van Bokhoven JA (2014) X-ray spectroscopy for chemical and energy sciences: the case of heterogeneous catalysis. J Synchrotron Radiat 21:1084–1089
158. Hitchcock AP, Toney MF (2014) Spectromicroscopy and coherent diffraction imaging: focus on energy materials applications. J Synchrotron Radiat 21:1019–1030
159. Kang HC, Yan H, Chu YS et al (2013) Oxidation of PtNi nanoparticles studied by a scanning X-ray fluorescence microscope with multi-layer Laue lenses. Nanoscale 5:7184–7187
160. Fraile Rodríguez A, Nolting F, Bansmann J et al (2007) X-ray imaging and spectroscopy of individual cobalt nanoparticles using photoemission electron microscopy. J Magn Magn Mater 316:426–428
161. Xin HL, Alayoglu S, Tao R et al (2014) Revealing the atomic restructuring of Pt–Co nanoparticles. Nano Lett 14:3203–3207
162. Vendelbo SB, Elkjær CF, Falsig H et al (2014) Visualization of oscillatory behaviour of Pt nanoparticles catalysing CO oxidation. Nat Mater 13:884–890
163. Billinge SJL, Levin I (2007) The problem with determining atomic structure at the nanoscale. Science 316:561–565
164. Zhao S, Li Y, Zakharov D et al Operando characterization of catalysts with a portable microreactor